

Competing charge-density wave instabilities in the kagome metal ScV_6Sn_6

Saizheng Cao,¹ Chenchao Xu,² Hiroshi Fukui,³ Taishun Manjo,³ Ming Shi,^{4,1} Yang Liu,¹ Chao Cao,^{1,*} and Yu Song^{1,†}

¹*Center for Correlated Matter and School of Physics, Zhejiang University, Hangzhou 310058, China*

²*Condensed Matter Group, Department of Physics,
Hangzhou Normal University, Hangzhou 310036, China*

³*Japan Synchrotron Radiation Research Institute,
SPring-8, 1-1-1 Kouto, Sayo, Hyogo 679-5198, Japan*

⁴*Photon Science Division, Paul Scherrer Institut, CH-5232 Villigen PSI, Switzerland*

Owing to its unique geometry, the kagome lattice hosts various many-body quantum states including frustrated magnetism, superconductivity, and charge-density waves (CDWs), with intense efforts focused on kagome metals exhibiting 2×2 CDWs associated with the nesting of van Hove saddle points. Recently, a $\sqrt{3} \times \sqrt{3}$ CDW was discovered in the kagome metal ScV_6Sn_6 below $T_{\text{CDW}} \approx 91$ K, whose underlying mechanism and formation process remain unclear. Using inelastic X-ray scattering, we discover a short-range $\sqrt{3} \times \sqrt{3} \times 2$ CDW that is dominant in ScV_6Sn_6 well above T_{CDW} , distinct from the $\sqrt{3} \times \sqrt{3} \times 3$ CDW below T_{CDW} . The short-range CDW grows upon cooling, and is accompanied by the softening of phonons, indicative of its dynamic nature. As the $\sqrt{3} \times \sqrt{3} \times 3$ CDW appears, the short-range CDW becomes suppressed, revealing a competition between these CDW instabilities. Our first-principles calculations indicate that the $\sqrt{3} \times \sqrt{3} \times 2$ CDW is energetically favored, consistent with experimental observations at high temperatures. However, the $\sqrt{3} \times \sqrt{3} \times 3$ CDW is selected as the ground state likely due to a large wavevector-dependent electron-phonon coupling, which also accounts for the enhanced electron scattering above T_{CDW} . The competing CDW instabilities in ScV_6Sn_6 lead to an unusual CDW formation process, with the most pronounced phonon softening and the static CDW occurring at different wavevectors.

INTRODUCTION

The unique geometry of the kagome lattice with corner-sharing triangles is amenable to realizing geometric frustration, Dirac cones, magnon and electronic topological flat bands, and van Hove singularities [1–13]. The combination of these ingredients leads to nontrivial electronic topology and correlated many-body states, as exemplified by the kagome metals AV_3Sb_5 ($A=\text{K}, \text{Rb}, \text{Cs}$) [14], which exhibit an unconventional charge-density wave (CDW) breaking both time-reversal and rotational symmetries [15–19], coexistent with a superconducting ground state [15, 20, 21]. Another example is the recently discovered CDW in the kagome metal FeGe , which develops in the presence of antiferromagnetic order and leads to an enhancement of the ordered moment [22, 23]. The CDW in both AV_3Sb_5 and FeGe are associated with a 2×2 in-plane ordering [15, 24–27], which is consistent with the nesting vector connecting neighboring van Hove singularities [28–30].

Recently, CDW was discovered in the bilayer kagome metal ScV_6Sn_6 [31], a member of the HfFe_6Ge_6 -type compounds. Similar to AV_3Sb_5 , V atoms in ScV_6Sn_6 form kagome layers with V-V distances in the range 2.73–2.75 Å, the V d -orbital bands cross the Fermi level, and there are no local moments [31]. In contrast to AV_3Sb_5 and FeGe , the V atoms in ScV_6Sn_6 form kagome bilayers [Fig. 1(a)], and the CDW is associated with a $\sqrt{3} \times \sqrt{3}$ in-plane ordering [Fig. 1(b)], and a tripling of the unit cell along the c -axis. Furthermore, whereas the CDW in AV_3Sb_5 is dominated by in-plane displacements of the V atoms [26] and hosts a superconducting ground state, the

CDW in ScV_6Sn_6 is mostly driven by displacements of the Sc and Sn atoms along the c -axis [31], and no superconductivity is observed up to pressures of 11 GPa [32]. Optical reflectivity measurements and electronic structure calculations indicate that the CDW in ScV_6Sn_6 is unlikely to result from Fermi-surface nesting, and the CDW does not exhibit a prominent charge gap formation [33], distinct from AV_3Sb_5 [34, 35]. This view is reinforced by electronic structure measurements, which in addition identify the lattice or a Lifshitz transition as instrumental for the CDW in ScV_6Sn_6 [36, 37].

Phonon measurements of the kagome metals AV_3Sb_5 and FeGe provided critical insights for understanding their respective CDWs [24, 38–40]. Whereas CDWs in both the weak- and strong-coupling limits are expected to exhibit soft phonons above the CDW ordering temperature, inelastic X-ray scattering (IXS) measurements of AV_3Sb_5 reveal an absence of such phonon softening, suggesting an unconventional CDW near the van Hove filling [24, 39]. Inelastic neutron scattering unveils the hardening of a longitudinal optical phonon inside the CDW state of CsV_3Sb_5 , implicating a key role of electron-phonon coupling in the CDW formation [38]. IXS measurements of FeGe uncover a charge dimerization and significant spin-phonon coupling, which intertwine with magnetism to drive the CDW formation [40]. In the case of ScV_6Sn_6 , theoretical calculations find competing lattice instabilities [41], which would lead to anomalies in the phonon spectra that need to be probed experimentally.

Here, we use IXS to study the lattice dynamics related to CDW formation in ScV_6Sn_6 , revealing a clear phonon softening above the first-order CDW ordering temper-

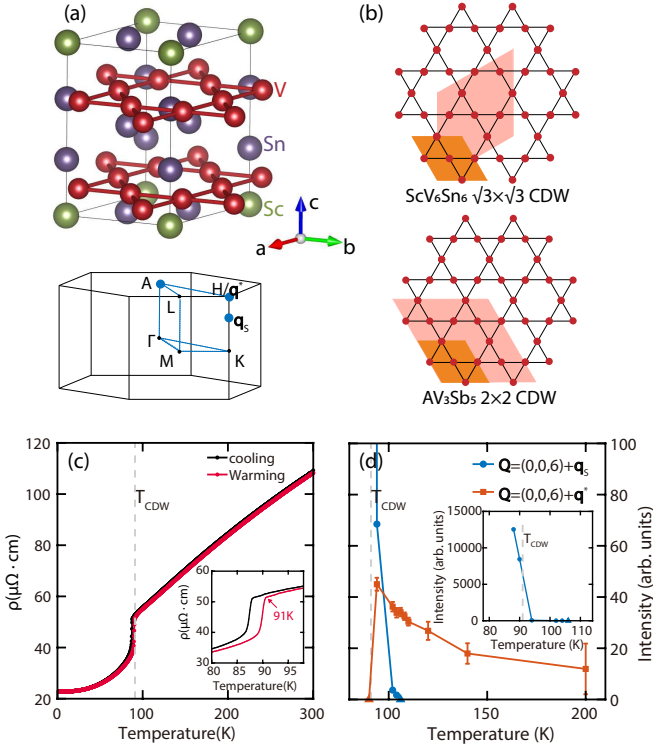


Figure 1. (a) Crystal structure of ScV₆Sn₆ [31], visualized using VESTA [42], with the Brillouin zone shown below. The blue circles are q -points probed in this work. (b) Expansion of the unit cell in the ab -plane for the CDWs in AV₃Sb₅ and ScV₆Sn₆. (c) The electrical resistivity of ScV₆Sn₆, the inset zooms in around T_{CDW} . (d) A comparison of the integrated intensities for q_s -CDW and q^* -CDW, obtained from l -scans centered at $(0,0,6)$. The inset zooms out to highlight the rapid growth of q_s -CDW. The triangles represent the absence of a detectable peak.

ature $T_{\text{CDW}} \approx 91$ K [Fig. 1(c)]. Whereas long-range static CDW order occurs at $q_s = (\frac{1}{3}, \frac{1}{3}, \frac{1}{3})$, corresponding to a $\sqrt{3} \times \sqrt{3} \times 3$ CDW (q_s -CDW), the phonon softening is most prominent at $q^* = (\frac{1}{3}, \frac{1}{3}, \frac{1}{2})$, corresponding to a short-range $\sqrt{3} \times \sqrt{3} \times 2$ CDW (q^* -CDW). q^* -CDW gains in intensity upon cooling, but becomes suppressed below T_{CDW} , replaced by q_s -CDW via a first-order transition [Fig. 1(d)]. First-principles calculations reveal that although q^* -CDW is energetically more favorable at the density functional theory level, a large q -dependent electron-phonon coupling selects q_s -CDW as the ground state, and also leads to strong electron scattering above T_{CDW} , accounting for the large resistivity drop upon cooling below T_{CDW} .

RESULTS

Competition between two distinct CDWs

Elastic scattering in ScV₆Sn₆ was measured by setting the energy transfer in IXS to zero, with results presented

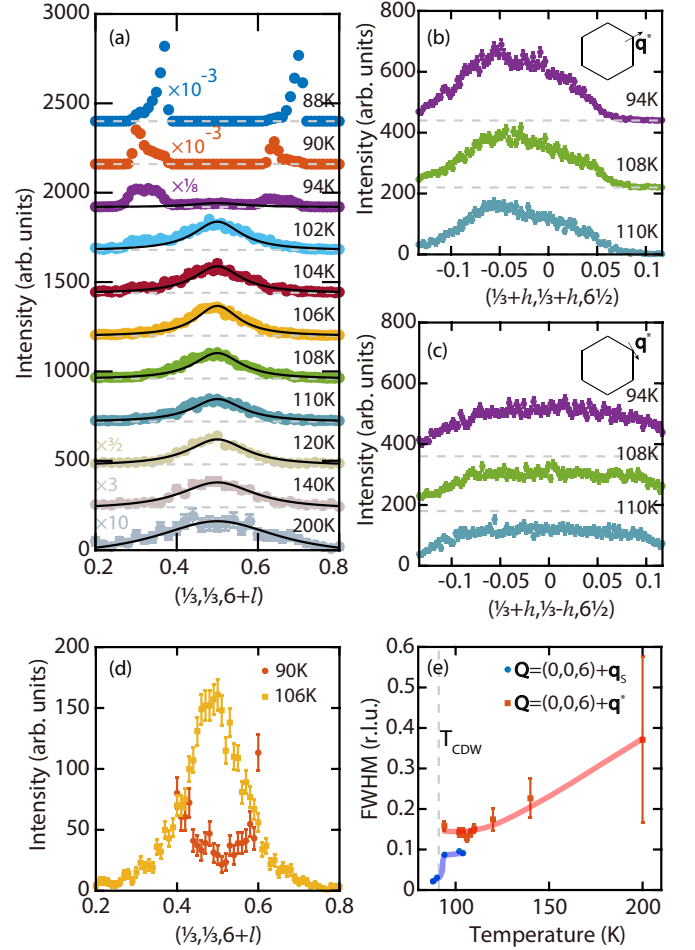


Figure 2. Elastic scans along (a) $(\frac{1}{3}, \frac{1}{3}, 6+l)$, (b) $(\frac{1}{3}+h, \frac{1}{3}+h, 6+\frac{1}{2})$, and (c) $(\frac{1}{3}+h, \frac{1}{3}-h, 6+\frac{1}{2})$, measured at various temperatures. The data have been shifted vertically (dashed gray lines) for clarity. The solid black lines in (a) are fits to the Lorentzian function. (d) A comparison between elastic scans along $(\frac{1}{3}, \frac{1}{3}, 6+l)$ between 90 K and 106 K. The scan at 90 K is limited in range as the scattering around $l = \frac{1}{3}$ and $\frac{2}{3}$ are too intense. (e) The FWHM along l for q_s -CDW and q^* -CDW as a function of temperature. The thick lines are guides to the eye.

in Fig. 2. For $T \gtrsim 100$ K, clear diffuse scattering centered around $(0,0,6) + q^*$ are observed in l -scans [Fig. 2(a)]. Scans along $(\frac{1}{3}+h, \frac{1}{3}+h, 6+\frac{1}{2})$ and $(\frac{1}{3}+h, \frac{1}{3}-h, 6+\frac{1}{2})$ confirm the short-range nature of these peaks along two orthogonal in-plane directions [Figs. 2(b) and (c)]. The q^* -CDW peak is significantly broader in the hk -plane than along l , and the peak asymmetry in Fig. 2(b) likely results from the variation in structure factors of the associated soft phonons in different Brillouin zones (Supplementary Note 1 and Supplementary Fig. 1). These diffuse scattering centered around $(0,0,6) + q^*$ evidence an unreported q^* -CDW in ScV₆Sn₆, distinct from q_s -CDW in its ground state [31]. As temperature is lowered, a weak peak around $(0,0,6) + q_s$ is first observed at 104 K, and quickly gains in intensity upon further cooling. In con-

trast, the \mathbf{q}^* -CDW peak at \mathbf{q}^* is no longer discernible at 90 K [Fig. 2(d)]. The temperature evolution of the integrated intensities are compared for \mathbf{q}_s -CDW and \mathbf{q}^* -CDW in Fig. 1(d), clearly revealing their competition. At $T = 88$ K (below T_{CDW}), the peak intensity of \mathbf{q}_s -CDW is at least 3 orders of magnitude larger than the maximum peak intensity of \mathbf{q}^* -CDW (occurring at ≈ 94 K), accounting for why only \mathbf{q}_s -CDW was detected in lab source X-ray diffraction measurements [31].

The full-widths at half-maximum (FWHM) of the measured CDW peaks along l are compared in Fig. 2(e), revealing that \mathbf{q}^* -CDW remains short-range down to 94 K. By fitting the Lorentzian function to l -scans of \mathbf{q}^* -CDW, we find the extracted correlation lengths is around 20 Å for $T \lesssim 110$ K. In the case of \mathbf{q}_s -CDW, the associated peaks are also broad for $T \gtrsim 100$ K, but sharpens for $T \lesssim 90$ K, with a correlation length exceeding 100 Å. We note the peaks associated with \mathbf{q}_s -CDW in Fig. 2(a) appear slightly away from \mathbf{q}_s in some measurements, which may result from a distribution of short-range \mathbf{q}_s -CDW clusters, or a small sample misalignment.

Lattice dynamics associated with the formation of CDWs

To probe the lattice dynamics associated with the CDW formation in ScV_6Sn_6 , IXS measurements were carried out at $(0, 0, 6) + \mathbf{q}_s$ and $(0, 0, 6) + \mathbf{q}^*$ [Figs. 3(a) and (b)], clearly revealing soft phonons at both positions. Whereas the soft phonons form two peaks centered around the elastic line at $T = 200$ K, they further soften upon cooling and form a single quasiselastic peak. To quantitatively analyze the phonon spectra, the phonon contributions in Figs. 3(a) and (b) are fit using the general DHO model:

$$S(E) = \frac{A}{1 - \exp(-\frac{E}{k_B T})} \frac{2}{\pi} \frac{\gamma E}{(E^2 - E_0^2)^2 + (E\gamma)^2},$$

shown as solid lines. In the DHO model, A is an intensity scale factor, E_0 is the undamped phonon energy, and γ is the damping rate (peak FWHM when $\gamma \ll E_0$). The fit values of E_0 decrease markedly with cooling for both \mathbf{q}_s and \mathbf{q}^* , with the phonons at \mathbf{q}^* softer than those at \mathbf{q}_s [Fig. 3(c)]. In contrast, the damping rate γ changes relatively little with temperature, with the phonons at \mathbf{q}_s slightly more strongly damped than those at \mathbf{q}^* . The observation of phonon softening in tandem with the growth of \mathbf{q}^* -CDW suggests it is dynamic in nature, and the diffuse character of \mathbf{q}^* -CDW is a result of softening over an extended region in momentum space. On the other hand, while \mathbf{q}_s -CDW develops at $T = 104$ K in the elastic channel [Fig. 2(a)], the corresponding \mathbf{q}_s phonon mode retains a well-defined energy at a similar temperature (105 K), indicating \mathbf{q}_s -CDW develops via the growth of a elastic

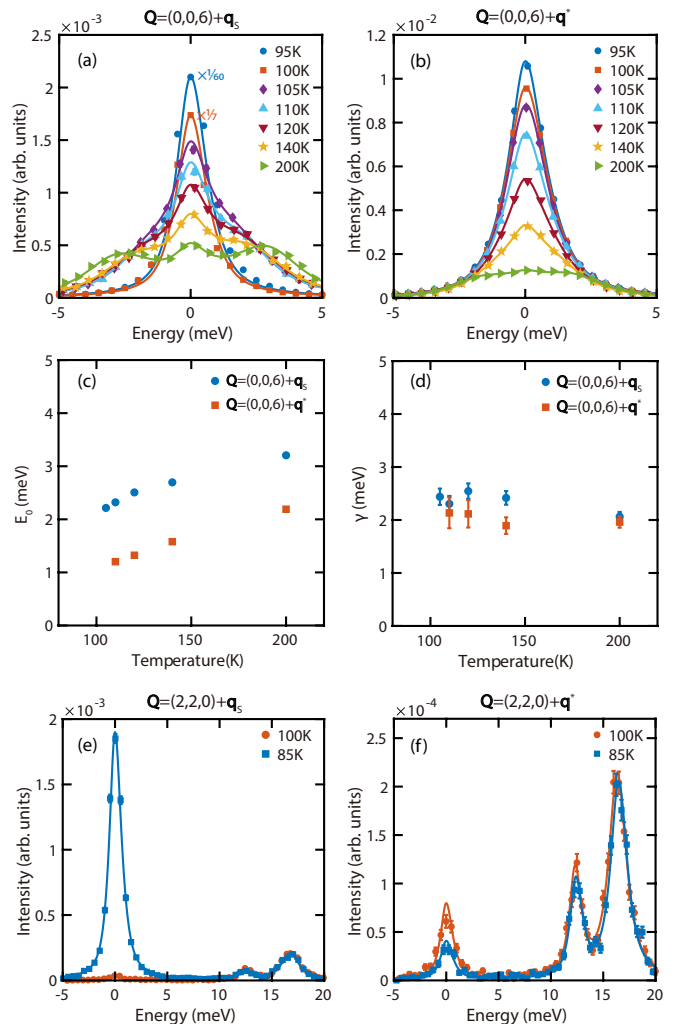


Figure 3. **Measurements of lattice dynamics in ScV_6Sn_6 .** IXS spectra at (a) $(0, 0, 6) + \mathbf{q}_s$ and (b) $(0, 0, 6) + \mathbf{q}^*$, measured at various temperatures. The solids lines are fits to a DHO and an elastic peak, convolved with the instrumental resolution. From these fits, (c) E_0 and (d) γ are extracted and compared between the two wavevectors. The 95 K and 100 K scans in (a) are resolution-limited. The 95 K, 100 K, and 105 K data in (b) contain an inelastic response but cannot be reliably distinguished from the elastic peak. DHO fit parameters are not shown for these scans. IXS spectra at (e) $(2, 2, 0) + \mathbf{q}_s$ and (f) $(2, 2, 0) + \mathbf{q}^*$, compared between 85 K and 100 K. The solids lines are fits to DHOs and an elastic peak, convolved with the instrumental resolution.

central peak, rather than phonons softening to zero energy. The short-range \mathbf{q}_s -CDW precursors detected at $T \gtrsim 100$ K [Figs. 2(a) and (e)] suggest the first-order transition at T_{CDW} is likely order-disorder type, as suggested for AV_3Sb_5 [39].

IXS measurements at \mathbf{q}_s and \mathbf{q}^* were also carried out in the (220) Brillouin zone [Figs. 3(e) and (f)], which is dominated by phonons polarized in the ab -plane. In contrast, measurements in the (006) Brillouin zone are dominated by c -axis polarized phonons. For both \mathbf{q}_s

and \mathbf{q}^* , soft phonons are hardly detectable in the (220) Brillouin zone, although the presence of \mathbf{q}^* -CDW is evidenced by the more intense elastic peak at 100 K relative to 85 K. For comparison, the elastic peak at \mathbf{q}_s gains in intensity upon cooling from 100 K to 85 K, due to the appearance of \mathbf{q}_s -CDW. The opposing temperature evolution of elastic peaks in Figs. 3(e) and (f) are consistent with the competition between \mathbf{q}_s -CDW and \mathbf{q}^* -CDW revealed in Fig. 2. The much weaker soft phonons in the (220) Brillouin zone suggest \mathbf{q}^* -CDW is associated with dominantly c -axis polarized lattice vibrations, similar to \mathbf{q}_s -CDW which is mostly due to Sc and Sn displacements along the c -axis [31]. Two additional phonon branches are also detected in Figs. 3(e) and (f), with phonon energies at \mathbf{q}_s slightly higher than those at \mathbf{q}^* . The fact these phonons hardly change across T_{CDW} suggest they are likely associated with in-plane vibrations of the lattice. Additional phonon modes that do not change significantly across T_{CDW} are also detected in several Brillouin zones (see Supplementary Note 2 and Supplementary Fig. 2), the energies of these phonon modes are shown in Fig. 4(d) and the Supplementary Fig. 3.

First-principles calculations

First-principles calculations were employed to understand the experimentally observed CDWs in ScV_6Sn_6 , with the calculated electronic structure shown in Fig. 4(a). We find the electronic structure close to the Fermi level is dominated by V-3d orbitals, which can also be seen in the projected density of states (DOS) [Fig. 4(b)], in agreement with previous study [41]. Characteristic features of the kagome lattice are identified in the electronic structure, including Dirac cones at K (~ 0.1 eV and -0.04 eV) and H (~ 0.5 eV), and topological flat bands around -0.5 eV at M and L , which manifest as van Hove-like features around -0.5 eV in the electronic DOS [Fig. 4(b)].

To probe the origins of the competing CDWs in ScV_6Sn_6 , the nesting function $J(\mathbf{q}) = \frac{1}{N_{\mathbf{k}}} \sum_{\nu, \mu, \mathbf{k}} \delta(\epsilon_{\mu\mathbf{k}}) \delta(\epsilon_{\nu\mathbf{k}+\mathbf{q}})$ is computed, where $\epsilon_{\mu\mathbf{k}}$ is the energy (with respect to the Fermi energy) of band μ at \mathbf{k} . As can be seen in Fig. 4(c), the most prominent feature of $J(\mathbf{q})$ is at the M -point, which does not correspond to a CDW instability [Fig. 4(d)], and multiple marginal features are observed in the $q_z = \frac{1}{3}$ and $\frac{1}{2}$ planes [Fig. 4(c)]. Most importantly, in the $q_z = \frac{1}{3}$ plane, no peak is present at $\mathbf{q}_s = (\frac{1}{3}, \frac{1}{3}, \frac{1}{3})$, suggesting that Fermi surface nesting is completely irrelevant in the formation of \mathbf{q}_s -CDW, consistent with previous findings [33, 41]. In the $q_z = \frac{1}{2}$ plane, hot spots are found around $(\frac{1}{6}, \frac{1}{6}, \frac{1}{2})$ and $\mathbf{q}^* = (\frac{1}{3}, \frac{1}{3}, \frac{1}{2})$, indicating a possible contribution of nesting towards \mathbf{q}^* -CDW. The results in Figs. 4(a)-(c) are obtained without spin-orbit coupling (SOC), and adding SOC leads to only marginal changes

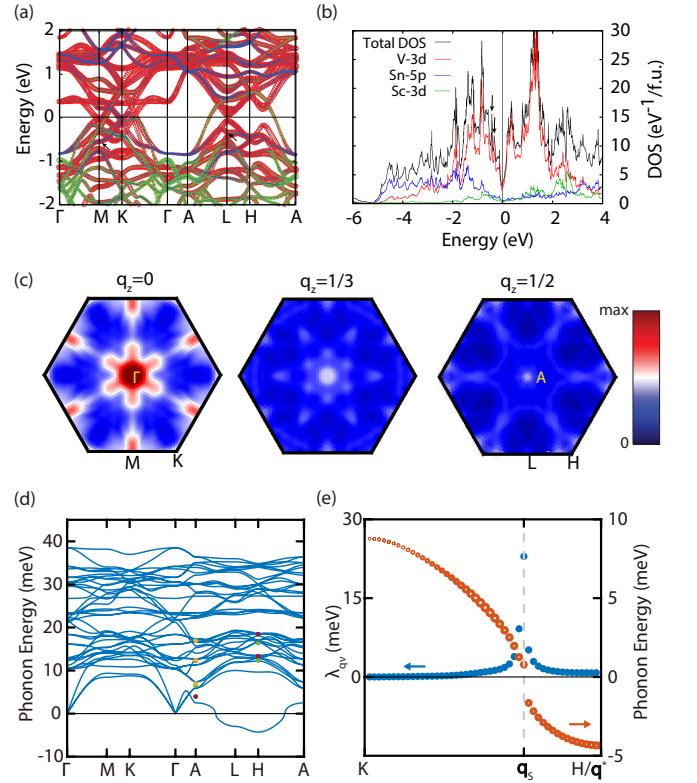


Figure 4. (a) Calculated electronic band structure of ScV_6Sn_6 with orbital characters, in the absence of spin-orbit interaction. Red corresponds to V-3d orbitals, blue Sc-3d orbitals, and green Sn-5p orbitals. The size of the circles represent the corresponding orbital weights. (b) Total and projected density of states (DOS), V-3d orbitals dominate within $E_F \pm 1$ eV. (c) Nesting functions calculated at $q_z = 0, 1/3$ and $1/2$. (d) The phonon spectrum of ScV_6Sn_6 calculated using DFPT. The red, green and yellow dots respectively represent phonon mode detected in (006), (220), and (300) Brillouin zones. (e) Calculated phonon dispersion (red symbols) and electron-phonon coupling strength $\lambda_{\mathbf{q}\nu}$ (blue symbols) for the soft phonon mode ($\nu = 1$) along $K - H$, the corresponding phonon self-energy $\Pi''_{\mathbf{q}\nu}$ is represented through the size of the red symbols.

(Supplementary Note 3 and Supplementary Figs. 4-5).

In addition to Fermi-surface nesting, electron-phonon coupling can also drive a CDW transition. To elucidate the role of phonons in the competing CDWs of ScV_6Sn_6 , we calculated its phonon spectrum using DFPT [43], shown in Fig. 4(d). The calculations reproduce several experimentally measured phonons modes at A and H [circles in Fig. 4(d)], demonstrating consistency between theory and experiment. In particular, several calculated phonon modes are nearly degenerate around 12.8 meV and 16.8 meV at H (\mathbf{q}^*), as well as around 13.0 meV and 17.0 meV at \mathbf{q}_s . These phonons match the experimental observations in Figs. 3(e) and (f), and are dominated by the in-plane motion of Sn atoms. Similar to previous calculations [41], imaginary phonon modes are present along $A - L - H$, with the imaginary A_1 mode at H

lowest in energy. In addition to the soft phonons experimentally observed at \mathbf{q}_s and \mathbf{q}^* , a low energy ~ 4.0 meV phonon mode without softening is detected experimentally at $A = (0, 0, \frac{1}{2})$, occurring at a higher energy than the calculated ~ 2.5 meV mode [Fig. 4(d)]. Furthermore, two new phonon modes are identified experimentally at A upon entering the \mathbf{q}_s -CDW state (Supplementary Note 2 and Supplementary Figs. 2-3).

In most cases, the imaginary phonon mode with the lowest energy would drive a CDW transition, which is clearly not the case in ScV₆Sn₆, since static CDW occurs at \mathbf{q}_s , rather than at \mathbf{q}^* (H) which has the lowest phonon mode. More surprisingly, our calculations indicate an absence of imaginary phonons at \mathbf{q}_s [Fig. 4(e)], suggesting that at the level of density functional theory, \mathbf{q}_s -CDW is also less competitive than the undistorted $P6/mmm$ structure. This is reflected in recovery of the undistorted structure, when relaxing the supercell modulated by the lowest energy phonon mode at \mathbf{q}_s (see Methods).

To address this problem, we calculated the phonon self-energy $\Pi''_{\mathbf{q}\nu}$ (inversely correlated with the phonon peak width in energy) and \mathbf{q} -dependent electron-phonon coupling strength $\lambda_{\mathbf{q}\nu}$ for the lowest phonon mode ($\nu = 1$) along K - H [44, 45] which are related to the electron-phonon coupling matrices $g''_{mn}(\mathbf{k}, \mathbf{q})$ via [44, 45]:

$$\Pi''_{\mathbf{q}\nu} = \text{Im} \left[\sum_{mn\mathbf{k}} |g''_{mn}(\mathbf{k}, \mathbf{q})|^2 \frac{f_{n\mathbf{k}} - f_{m\mathbf{k}+\mathbf{q}}}{\epsilon_{n\mathbf{k}} - \epsilon_{m\mathbf{k}+\mathbf{q}} - \omega_{\mathbf{q}\nu} + i\eta} \right],$$

and

$$\lambda_{\mathbf{q}\nu} = \frac{1}{N_F \omega_{\mathbf{q}\nu}} \sum_{mn\mathbf{k}} |g''_{mn}(\mathbf{k}, \mathbf{q})|^2 \delta(\epsilon_{n\mathbf{k}}) \delta(\epsilon_{m\mathbf{k}+\mathbf{q}}).$$

We find $\Pi''_{\mathbf{q}}$ for the soft mode increases from K to H [Fig. 4(e)], with its value at \mathbf{q}_s slightly smaller than that at \mathbf{q}^* , consistent with the experimental values of γ (positively correlated with the phonon peak width in energy) being slightly larger at \mathbf{q}_s than at \mathbf{q}^* [Fig. 3(d)]. A sharp peak is observed for $\lambda_{\mathbf{q}\nu}$ at $\mathbf{q}_s = (\frac{1}{3}, \frac{1}{3}, \frac{1}{3})$ [Fig. 4(e)], indicating a remarkably large \mathbf{q} -dependent electron-phonon coupling. The calculated electron-phonon coupling constant $\lambda_{\mathbf{q}\nu}$ for the soft phonon mode at \mathbf{q}_s is around 32 meV, which is over 20 times the value at \mathbf{q}^* (~ 1.32 meV), and more than 7 times the imaginary phonon mode energy at \mathbf{q}^* (~ 4.35 meV). The absence of features in the nesting function [Fig. 4(c)] and the presence of a giant electron-phonon at \mathbf{q}_s [Fig. 4(e)], both strongly indicate the latter is responsible for selecting \mathbf{q}_s -CDW as the ground state in ScV₆Sn₆.

DISCUSSION

CDWs usually occur via phonon softening, corresponding to coherent lattice oscillations that gradually become

more competitive in energy, or the growth of a central peak that reflect the ordering of local CDW patches. The development of CDWs in one dimension as modeled by Peierls [46], and in two-dimensional systems such as $2H$ -NbSe₂ [47] and BaNi₂As₂ [48, 49], are accompanied by prominent phonon softening. While such phonon softening is limited to small range in momentum in Peierls' model, it occurs over an extended range in $2H$ -NbSe₂ and BaNi₂As₂, similar to the observed behavior of \mathbf{q}^* -CDW in ScV₆Sn₆. On the other hand, order-disorder CDW transitions have been reported in systems such as (Ca_{1-x}Sr_x)₃Rh₄Sn₁₃ [50] and AV₃Sb₅ [39], and likely characterizes the formation of \mathbf{q}_s -CDW in ScV₆Sn₆. Thus, the CDW formation process in ScV₆Sn₆ is unique in that both prominent phonon softening and the growth of a central peak are observed, with the two effects associated with different wavevectors, a result of competing CDW instabilities.

There are three implications that directly result from our experiments and first-principles calculations. Firstly, while \mathbf{q}^* -CDW is energetically favored in DFT calculations, \mathbf{q}_s -CDW is the ground state of ScV₆Sn₆. To reconcile this apparent inconsistency, we note the calculated electronic states and phonon energies are “bare” particles, without full consideration of electron-phonon coupling, which leads to considerable electron/phonon self-energies in the strong-coupling limit. We argue that if the phonon induced electronic self-energy is properly taken into consideration in many-body theories beyond DFT, \mathbf{q}_s -CDW should become energetically more competitive than \mathbf{q}^* -CDW. Secondly, both \mathbf{q}_s -CDW and \mathbf{q}^* -CDW are associated with the A_1 phonon mode, for which the V kagome lattice is mostly unaffected. Since the electronic states near the Fermi level are dominated by the V - $3d$ orbitals, gap-opening associated with either \mathbf{q}_s -CDW or \mathbf{q}^* -CDW is unlikely to be prominent in ScV₆Sn₆. Thirdly, our findings explain the substantial drop of resistivity below T_{CDW} [Fig. 1(c)]: the large electron-phonon coupling and extended phonon softening revealed in this work both enhance electron scattering above T_{CDW} , and the removal of these effects below T_{CDW} strongly reduces electron scattering, consistent with optical conductivity measurements [33].

Furthermore, it is interesting to consider whether the competition between CDW instabilities in ScV₆Sn₆ could be tilted in favor of \mathbf{q}^* -CDW via external tuning. In this regard, electrical transport measurements in pressurized ScV₆Sn₆ reveal that the sharp drop in resistivity associated with \mathbf{q}_s -CDW persists up to ~ 2.0 GPa, beyond which it is suddenly replaced by a much weaker kink in resistivity, before becoming fully suppressed at ~ 2.4 GPa [32]. The sudden qualitative change in resistivity anomaly above ~ 2.0 GPa is suggestive of a change in the ground state, and the much less pronounced resistivity anomaly between ~ 2.0 GPa and ~ 2.4 GPa suggests the associated transition being second-order.

In such a scenario, a distinct possibility is that \mathbf{q}^* -CDW becomes the ground state between ~ 2.0 GPa and ~ 2.4 GPa, and since \mathbf{q}^* -CDW develops through phonon-softening [Fig. 3] as in $2H$ -NbSe₂ [47] and BaNi₂As₂ [48, 49], the corresponding resistivity anomaly would be likewise rather subtle.

In conclusion, we uncovered competing CDW instabilities in the kagome metal ScV₆Sn₆, which lead to a unique CDW formation process with the dominant soft phonons and the ground state CDW occurring at different wavevectors, distinct from typical phonon-driven CDWs. The two CDWs develop in highly different manners, suggestive of distinct mechanisms, and differentiates ScV₆Sn₆ from CDWs in other kagome metals. As the \mathbf{q}_s -CDW ground state is not captured in first-principles DFT calculations, it is likely a many-body effect driven by a giant \mathbf{q} -dependent electron-phonon coupling. Our findings demonstrate a strong electron-phonon coupling on the kagome lattice could lead to nearly degenerate ground states, a setup primed for the emergence of unusual phases of matter.

METHODS

Experimental details

Single crystals of ScV₆Sn₆ were grown using the self-flux method with Sc:V:Sn = 1:6:40 [31]. Distilled scandium pieces (99.9%), vanadium pieces (99.7%), and tin shot (99.99+%) were placed in an alumina crucible and sealed under vacuum in a quartz ampoule. The ampoule was placed in a furnace and heated to 1150 °C for 12 hours, then held at 1150 °C for 20 hours. The sample was then cooled to 750 °C at a rate of 1 °C/h, at which point the excess Sn flux was removed with the aid of a centrifuge. The resulting crystals are plate-like with the c -axis normal to the plates, and typical sample dimensions are around $1 \times 1 \times 0.5$ mm³. Electrical resistivity was measured with the standard four-point method.

Inelastic X-ray scattering measurements were carried out in the transmission geometry using the BL35XU beamline [51] at SPring-8, Japan. The incident photon energy is 21.7476 keV. A ~ 70 μm thick sample [Supplementary Fig. 6(a)], comparable to the attenuation length of ~ 20 keV X-rays in ScV₆Sn₆, was prepared and mounted on a Cu post using silver epoxy. The instrumental energy resolution was measured using a piece of polymethyl methacrylate (PMMA), and parametrized using a pseudo-Voigt function. The instrumental resolution function $R(E)$ is then obtained by normalizing the pseudo-Voigt function to unit area [Supplementary Fig. 6(b)]. The full-width at half maximum (FWHM) of $R(E)$ is ~ 1.38 meV. For temperatures around T_{CDW} , measurements were consistently carried out upon warming. Momentum transfer is referenced in reciprocal lattice units,

using the high-temperature hexagonal $P6/mmm$ cell of ScV₆Sn₆, with $a = b \approx 5.47$ Å and $c \approx 9.16$ Å [31]. All measured scattering intensities are normalized by a monitor right before the sample. For momentum scans of elastic scattering, an attenuator was used to avoid saturating the detector when needed, which can be corrected for via the calibrated attenuation of the attenuator. These corrections have been applied to the data in Fig. 2.

Analysis of the experimental data

The elastic scans in momentum around \mathbf{q}^* are fit to a Lorentzian function:

$$I(\mathbf{Q}) = b + \frac{A}{\pi} \frac{\frac{\Gamma}{2}}{(\mathbf{Q} - \mathbf{Q}^*)^2 + (\frac{\Gamma}{2})^2},$$

where b is a small constant, A is the integrated area, $\mathbf{Q}^* = (0, 0, 6) + \mathbf{q}^*$ is the center of peak, and Γ is the full-width at half-maximum (FWHM). For temperatures with detectable \mathbf{q}_s -CDW intensity, regions around $(\frac{1}{3}, \frac{1}{3}, 6\frac{1}{3})$ and $(\frac{1}{3}, \frac{1}{3}, 6\frac{2}{3})$ are masked in the fit. Integrated intensities and FWHMs for \mathbf{q}_s -CDW are then determined numerically from the data around $(\frac{1}{3}, \frac{1}{3}, 6\frac{1}{3})$, after subtracting the fit to the Lorentzian function. For temperatures without detectable \mathbf{q}^* -CDW, the integrated intensities and FWHMs for \mathbf{q}_s -CDW are likewise obtained numerically, after subtracting a small constant term determined from the mean of data points away from the \mathbf{q}^* -CDW peaks. The obtained integrated intensities and FWHMs for \mathbf{q}_s -CDW and \mathbf{q}^* -CDW are shown in Figs. 1(d) and Fig. 2(e).

Using the least squares method, all measured experimental phonon intensities are fit to the expression:

$$I(E) = b + cR(E - \delta E) + \sum_{i=1}^n \int_{-\infty}^{\infty} [S_i(E - \delta E - E')] R(E') dE',$$

where n is the minimum number of phonon modes that capture the experimentally measured data, and the integrals correspond to convolutions with the instrumental resolution $R(E)$. In practice, since $R(E)$ has a FWHM of ~ 1.38 meV, the integrals are numerically carried out in the energy range $[-20, 20]$ meV. The above equation contains a small constant term b , a resolution-limited elastic peak $cR(E)$ and n general damped harmonic oscillators (DHOs) [52, 53], with each phonon mode represented by the DHO $S_i(E)$:

$$S_i(E) = \frac{A_i}{1 - \exp(-\frac{E}{k_B T})} \frac{2}{\pi} \frac{\gamma_i E}{(E^2 - E_{0i}^2)^2 + (E\gamma_i)^2},$$

where A_i is the intensity scale factor, E_{0i} is the phonon energy in the absence of damping, and γ_i is the damping rate, all for phonon mode i . In the limit of $\gamma_i \rightarrow 0$ (or the

phonon mode is resolution-limited), the above equation for $S_i(E)$ can be replaced by:

$$S_i(E) = \frac{A_i}{1 - \exp(-\frac{E}{k_B T})} \frac{\delta(E - E_{0i}) - \delta(E + E_{0i})}{E}.$$

In addition, the difference between the actual zero energy and the nominal zero energy, is contained in our model as a free parameter δE to account for shifts in energy between different scans. Possible shifts of energy within each scan is considered to be negligible and ignored in our analysis. The data in Fig. 3 and Supplementary Fig. 2 have been shifted by δE obtained in the fits.

As temperature is cooled and \mathbf{q}_s -CDW develops, phonons at \mathbf{q}_s become difficult to measure due to the elastic tail of the \mathbf{q}_s -CDW peak. A result of this is that the 95 K and 100 K data become almost resolution-limited around the elastic line, and no phonons are contained in the corresponding fits [Fig. 3(a) and Supplementary Fig. 7(a)]. One the other hand, while the soft phonon mode at \mathbf{q}^* becomes a single peak centered around the elastic peak at 95 K, 100 K, and 105 K, they are broader in energy than the instrumental resolution [Fig. 3(b) and Supplementary Fig. 7(b)]. Although these soft phonons can be described by the DHO model, it is not possible to reliably extract E_{0i} and γ_i .

First-principles calculations

Electronic structure calculations were carried out using density functional theory (DFT) implemented in **Quantum Espresso** [54]. The exchange-correlations function was taken within the generalized gradient approximation (GGA) in the parameterization of Perdew, Burke and Ernzerhof [55]. The energy cutoff of plane-wave basis was up to 64 Ry (720 Ry for the augmentation charge). The 3s, 3p, 3d, 4s electrons for Sc and V atoms and 4d, 5s, and 5p electrons for Sn are considered as valence electrons in the employed pseudopotentials. For the undistorted structures, the charge density was calculated self-consistently with a Γ -centered $12 \times 12 \times 6$ \mathbf{k} -point mesh. The lattice constants and atomic coordinates were fully relaxed until the force on each atom was less than 1 meV/Å and the internal stress less than 0.1 kbar.

The bare electronic susceptibility was calculated with the Lindhard formula:

$$\chi_0(\omega, \mathbf{q}) = -\frac{1}{N_{\mathbf{k}}} \sum_{\mu\nu\mathbf{k}} \frac{f(\varepsilon_{\nu\mathbf{k}+\mathbf{q}}) - f(\varepsilon_{\mu\mathbf{k}})}{\omega + \varepsilon_{\nu\mathbf{k}+\mathbf{q}} - \varepsilon_{\mu\mathbf{k}} + i0^+},$$

where μ, ν are band indexes, $\varepsilon_{\mu\mathbf{k}}$ is the energy eigenvalue of band μ at \mathbf{k} , $f(\varepsilon_{\mu\mathbf{k}})$ is the Fermi-Dirac distribution.

The imaginary part of the bare electron susceptibility ($\chi_0''(\omega, \mathbf{q})$) is related to the nesting function $J(\mathbf{q})$ through:

$$J(\mathbf{q}) = \lim_{\omega \rightarrow 0} \frac{\chi_0''(\omega)}{\omega} = \frac{1}{N_{\mathbf{k}}} \sum_{\nu, \mu, \mathbf{k}} \delta(\varepsilon_{\mu\mathbf{k}}) \delta(\varepsilon_{\nu\mathbf{k}+\mathbf{q}}).$$

The phonon spectrum is calculated using density functional perturbation theory (DFPT) [43] on a $4 \times 4 \times 3$ \mathbf{q} -grid. The electron-phonon coupling strength $\lambda_{\mathbf{q}\nu}$ and phonon self-energy $\Pi''_{\mathbf{q}\nu}$ were calculated on a $48 \times 48 \times 24$ Wannier-interpolated \mathbf{k} -grid using the EPW package [45]. Bands derived from Sc-3d, V-3d and Sb-5p orbitals from DFT calculations were fit to a tight-binding Hamiltonian using the Maximally-Projected Wannier Functions method [Supplementary Fig. 8], which were then used in the EPW calculations [44].

We have also performed calculations for the distorted structures associated with \mathbf{q}^* - and \mathbf{q}_s -CDWs. For \mathbf{q}^* -CDW, the initial structure was obtained by imposing the lowest energy phonon mode (A_1) modulation on a $3 \times 3 \times 2$ supercell. For \mathbf{q}_s -CDW, the initial structure was obtained by imposing the lowest energy phonon mode modulation on a rhombohedral supercell with lattice vectors $\mathbf{A}'_1 = \mathbf{A}_1 + \mathbf{A}_3$, $\mathbf{A}'_2 = \mathbf{A}_2 + \mathbf{A}_3$ and $\mathbf{A}'_3 = -(\mathbf{A}_1 + \mathbf{A}_2) + \mathbf{A}_3$, where \mathbf{A}_i are the lattice vectors for the undistorted $P6/mmm$ structure ($\mathbf{A}_3 \perp \mathbf{A}_{1,2}$ and $\angle(\mathbf{A}_1, \mathbf{A}_2) = 120^\circ$). See Supplementary Fig. 9 for a comparison between unit cells for the undistorted $P6/mmm$ structure and the rhombohedral structure. The initial structures were then fully relaxed so that the force on each atom is less than 1 meV/Å and the internal stress less than 0.1 kbar. The fully relaxed \mathbf{q}^* -structure is ~ 7.5 meV/f.u. lower in energy than the undistorted structure, whereas the \mathbf{q}_s -structure relaxes back to the undistorted $P6/mmm$ structure, consistent with our calculations that show an absence of imaginary phonon at \mathbf{q}_s .

DATA AVAILABILITY

All relevant data are available from the corresponding authors upon request.

ACKNOWLEDGEMENTS

The work at Zhejiang University was supported by the National Key R&D Program of China (No. 2022YFA1402200), the Pioneer and Leading Goose R&D Program of Zhejiang (2022SDXHDX0005), the Key R&D Program of Zhejiang Province, China (2021C01002), and the National Natural Science Foundation of China (No. 12274363, 12274364). Measurements at the BL35XU of SPring-8 were performed with the approval of JASRI (Proposal No. 2022B1283). The calculations were performed on the HPC facility at the Center

for Correlated Matter, and partially on the HPCC at Hangzhou Normal University.

* ccao@zju.edu.cn

† yusong_phys@zju.edu.cn

- [1] I. Syozi, *Progress of Theoretical Physics* **6**, 306 (1951).
- [2] T.-H. Han, J. S. Helton, S. Chu, D. G. Nocera, J. A. Rodriguez-Rivera, C. Broholm, and Y. S. Lee, *Nature* **492**, 406 (2012).
- [3] C. Broholm, R. J. Cava, S. A. Kivelson, D. G. Nocera, M. R. Norman, and T. Senthil, *Science* **367**, eaay0668 (2020).
- [4] L. Ye, M. Kang, J. Liu, F. von Cube, C. R. Wicker, T. Suzuki, C. Jozwiak, A. Bostwick, E. Rotenberg, D. C. Bell, L. Fu, R. Comin, and J. G. Checkelsky, *Nature* **555**, 638 (2018).
- [5] E. Liu, Y. Sun, N. Kumar, L. Muechler, A. Sun, L. Jiao, S.-Y. Yang, D. Liu, A. Liang, Q. Xu, J. Kroder, V. Stüß, H. Borrmann, C. Shekhar, Z. Wang, C. Xi, W. Wang, W. Schnelle, S. Wirth, Y. Chen, S. T. B. Goennenwein, and C. Felser, *Nature Physics* **14**, 1125 (2018).
- [6] M. Kang, L. Ye, S. Fang, J.-S. You, A. Levitan, M. Han, J. I. Facio, C. Jozwiak, A. Bostwick, E. Rotenberg, M. K. Chan, R. D. McDonald, D. Graf, K. Kaznatcheev, E. Vescovo, D. C. Bell, E. Kaxiras, J. van den Brink, M. Richter, M. P. Ghimire, J. G. Checkelsky, and R. Comin, *Nature Materials* **19**, 163 (2019).
- [7] Z. Lin, J.-H. Choi, Q. Zhang, W. Qin, S. Yi, P. Wang, L. Li, Y. Wang, H. Zhang, Z. Sun, L. Wei, S. Zhang, T. Guo, Q. Lu, J.-H. Cho, C. Zeng, and Z. Zhang, *Phys. Rev. Lett.* **121**, 096401 (2018).
- [8] J.-X. Yin, S. S. Zhang, G. Chang, Q. Wang, S. S. Tsirkin, Z. Guguchia, B. Lian, H. Zhou, K. Jiang, I. Belopolski, N. Shumiya, D. Multer, M. Litskevich, T. A. Cochran, H. Lin, Z. Wang, T. Neupert, S. Jia, H. Lei, and M. Z. Hasan, *Nature Physics* **15**, 443 (2019).
- [9] A. B. Harris, C. Kallin, and A. J. Berlinsky, *Phys. Rev. B* **45**, 2899 (1992).
- [10] K. Matan, D. Grohol, D. G. Nocera, T. Yildirim, A. B. Harris, S. H. Lee, S. E. Nagler, and Y. S. Lee, *Phys. Rev. Lett.* **96**, 247201 (2006).
- [11] R. Chisnell, J. S. Helton, D. E. Freedman, D. K. Singh, R. I. Bewley, D. G. Nocera, and Y. S. Lee, *Phys. Rev. Lett.* **115**, 147201 (2015).
- [12] K. Jiang, T. Wu, J.-X. Yin, Z. Wang, M. Z. Hasan, S. D. Wilson, X. Chen, and J. Hu, *National Science Review* **10**, nwac199 (2022).
- [13] J.-X. Yin, B. Lian, and M. Z. Hasan, *Nature* **612**, 647–657 (2022).
- [14] B. R. Ortiz, L. C. Gomes, J. R. Morey, M. Winiarski, M. Bordelon, J. S. Mangum, I. W. H. Oswald, J. A. Rodriguez-Rivera, J. R. Neilson, S. D. Wilson, E. Ertekin, T. M. McQueen, and E. S. Toberer, *Phys. Rev. Mater.* **3**, 094407 (2019).
- [15] B. R. Ortiz, S. M. L. Teicher, Y. Hu, J. L. Zuo, P. M. Sarte, E. C. Schueller, A. M. M. Abeykoon, M. J. Krogstad, S. Rosenkranz, R. Osborn, R. Seshadri, L. Balents, J. He, and S. D. Wilson, *Phys. Rev. Lett.* **125**, 247002 (2020).
- [16] C. Mielke, D. Das, J.-X. Yin, H. Liu, R. Gupta, Y.-X. Jiang, M. Medarde, X. Wu, H. C. Lei, J. Chang, P. Dai, Q. Si, H. Miao, R. Thomale, T. Neupert, Y. Shi, R. Khasanov, M. Z. Hasan, H. Luetkens, and Z. Guguchia, *Nature* **602**, 245 (2022).
- [17] Y.-X. Jiang, J.-X. Yin, M. M. Denner, N. Shumiya, B. R. Ortiz, G. Xu, Z. Guguchia, J. He, M. S. Hossain, X. Liu, J. Ruff, L. Kautzsch, S. S. Zhang, G. Chang, I. Belopolski, Q. Zhang, T. A. Cochran, D. Multer, M. Litskevich, Z.-J. Cheng, X. P. Yang, Z. Wang, R. Thomale, T. Neupert, S. D. Wilson, and M. Z. Hasan, *Nature Materials* **20**, 1353 (2021).
- [18] L. Nie, K. Sun, W. Ma, D. Song, L. Zheng, Z. Liang, P. Wu, F. Yu, J. Li, M. Shan, D. Zhao, S. Li, B. Kang, Z. Wu, Y. Zhou, K. Liu, Z. Xiang, J. Ying, Z. Wang, T. Wu, and X. Chen, *Nature* **604**, 59 (2022).
- [19] H. Li, H. Zhao, B. R. Ortiz, T. Park, M. Ye, L. Balents, Z. Wang, S. D. Wilson, and I. Zeljkovic, *Nature Physics* **18**, 265 (2022).
- [20] B. R. Ortiz, P. M. Sarte, E. M. Kenney, M. J. Graf, S. M. L. Teicher, R. Seshadri, and S. D. Wilson, *Phys. Rev. Materials* **5**, 034801 (2021).
- [21] Q. Yin, Z. Tu, C. Gong, Y. Fu, S. Yan, and H. Lei, *Chinese Physics Letters* **38**, 037403 (2021).
- [22] X. Teng, L. Chen, F. Ye, E. Rosenberg, Z. Liu, J.-X. Yin, Y.-X. Jiang, J. S. Oh, M. Z. Hasan, K. J. Neubauer, B. Gao, Y. Xie, M. Hashimoto, D. Lu, C. Jozwiak, A. Bostwick, E. Rotenberg, R. J. Birgeneau, J.-H. Chu, M. Yi, and P. Dai, *Nature* **609**, 490 (2022).
- [23] J.-X. Yin, Y.-X. Jiang, X. Teng, M. S. Hossain, S. Mardanya, T.-R. Chang, Z. Ye, G. Xu, M. M. Denner, T. Neupert, B. Lienhard, H.-B. Deng, C. Setty, Q. Si, G. Chang, Z. Guguchia, B. Gao, N. Shumiya, Q. Zhang, T. A. Cochran, D. Multer, M. Yi, P. Dai, and M. Z. Hasan, *Phys. Rev. Lett.* **129**, 166401 (2022).
- [24] H. Li, T. T. Zhang, T. Yilmaz, Y. Y. Pai, C. E. Marvinney, A. Said, Q. W. Yin, C. S. Gong, Z. J. Tu, E. Vescovo, C. S. Nelson, R. G. Moore, S. Murakami, H. C. Lei, H. N. Lee, B. J. Lawrie, and H. Miao, *Phys. Rev. X* **11**, 031050 (2021).
- [25] Z. Liang, X. Hou, F. Zhang, W. Ma, P. Wu, Z. Zhang, F. Yu, J.-J. Ying, K. Jiang, L. Shan, Z. Wang, and X.-H. Chen, *Phys. Rev. X* **11**, 031026 (2021).
- [26] B. R. Ortiz, S. M. L. Teicher, L. Kautzsch, P. M. Sarte, N. Ratcliff, J. Harter, J. P. C. Ruff, R. Seshadri, and S. D. Wilson, *Phys. Rev. X* **11**, 041030 (2021).
- [27] Q. Stahl, D. Chen, T. Ritschel, C. Shekhar, E. Sadrollahi, M. C. Rahn, O. Ivashko, M. v. Zimmermann, C. Felser, and J. Geck, *Phys. Rev. B* **105**, 195136 (2022).
- [28] M. Kang, S. Fang, J.-K. Kim, B. R. Ortiz, S. H. Ryu, J. Kim, J. Yoo, G. Sangiovanni, D. D. Sante, B.-G. Park, C. Jozwiak, A. Bostwick, E. Rotenberg, E. Kaxiras, S. D. Wilson, J.-H. Park, and R. Comin, *Nature Physics* **18**, 301 (2022).
- [29] Y. Hu, X. Wu, B. R. Ortiz, S. Ju, X. Han, J. Ma, N. C. Plumb, M. Radovic, R. Thomale, S. D. Wilson, A. P. Schnyder, and M. Shi, *Nature Communications* **13**, 2220 (2022).
- [30] X. Teng, J. S. Oh, H. Tan, L. Chen, J. Huang, B. Gao, J.-X. Yin, J.-H. Chu, M. Hashimoto, D. Lu, C. Jozwiak, A. Bostwick, E. Rotenberg, G. E. Granroth, B. Yan, R. J. Birgeneau, P. Dai, and M. Yi, *Nature Physics* (2023).
- [31] H. W. S. Arachchige, W. R. Meier, M. Marshall, T. Mat-suoka, R. Xue, M. A. McGuire, R. P. Hermann, H. Cao,

- and D. Mandrus, *Phys. Rev. Lett.* **129**, 216402 (2022).
- [32] X. Zhang, J. Hou, W. Xia, Z. Xu, P. Yang, A. Wang, Z. Liu, J. Shen, H. Zhang, X. Dong, Y. Uwamoto, J. Sun, B. Wang, Y. Guo, and J. Cheng, *Materials* **15**, 7372 (2022).
- [33] T. Hu, H. Pi, S. Xu, L. Yue, Q. Wu, Q. Liu, S. Zhang, R. Li, X. Zhou, J. Yuan, D. Wu, T. Dong, H. Weng, and N. Wang, [arXiv:2211.03412](https://arxiv.org/abs/2211.03412).
- [34] X. Zhou, Y. Li, X. Fan, J. Hao, Y. Dai, Z. Wang, Y. Yao, and H.-H. Wen, *Phys. Rev. B* **104**, L041101 (2021).
- [35] E. Uykur, B. R. Ortiz, O. Iakutkina, M. Wenzel, S. D. Wilson, M. Dressel, and A. A. Tsirlin, *Phys. Rev. B* **104**, 045130 (2021).
- [36] M. Tuniz, A. Consiglio, D. Puntel, C. Bigi, S. Enzner, G. Pokharel, P. Orgiani, W. Bronsch, F. Parmigiani, V. Polewczyk, P. D. C. King, J. W. Wells, I. Zeljkovic, P. Carrara, G. Rossi, J. Fujii, I. Vobornik, S. D. Wilson, R. Thomale, T. Wehling, G. Sangiovanni, G. Panaccione, F. Cilento, D. D. Sante, and F. Mazzola, [arXiv:2302.10699](https://arxiv.org/abs/2302.10699).
- [37] S.-H. Kang, H. Li, W. R. Meier, J. W. Villanova, S. Hus, H. Jeon, H. W. S. Arachchige, Q. Lu, Z. Gai, J. Denlinger, R. Moore, M. Yoon, and D. Mandrus, [arXiv:2302.14041](https://arxiv.org/abs/2302.14041).
- [38] Y. Xie, Y. Li, P. Bourges, A. Ivanov, Z. Ye, J.-X. Yin, M. Z. Hasan, A. Luo, Y. Yao, Z. Wang, G. Xu, and P. Dai, *Phys. Rev. B* **105**, L140501 (2022).
- [39] D. Subires, A. Korshunov, A. H. Said, L. Sánchez, B. R. Ortiz, S. D. Wilson, A. Bosak, and S. Blanco-Canosa, *Nature Communications* **14**, 1015 (2023).
- [40] H. Miao, T. T. Zhang, H. X. Li, G. Fabbris, A. H. Said, R. Tartaglia, T. Yilmaz, E. Vescovo, J. X. Yin, S. Murakami, L. X. Feng, K. Jiang, X. L. Wu, A. F. Wang, S. Okamoto, Y. L. Wang, and H. N. Lee, [arXiv:2210.06359](https://arxiv.org/abs/2210.06359).
- [41] H. Tan and B. Yan, [arXiv:2302.07922](https://arxiv.org/abs/2302.07922).
- [42] K. Momma and F. Izumi, *Journal of Applied Crystallography* **41**, 653 (2008).
- [43] F. Giustino, *Rev. Mod. Phys.* **89**, 015003 (2017).
- [44] F. Giustino, M. L. Cohen, and S. G. Louie, *Phys. Rev. B* **76**, 165108 (2007).
- [45] J. Noffsinger, F. Giustino, B. D. Malone, C.-H. Park, S. G. Louie, and M. L. Cohen, *Computer Physics Communications* **181**, 2140 (2010).
- [46] X. Zhu, J. Guo, J. Zhang, and E. W. Plummer, *Advances in Physics: X* **2**, 622 (2017).
- [47] F. Weber, S. Rosenkranz, J.-P. Castellan, R. Osborn, R. Hott, R. Heid, K.-P. Bohnen, T. Egami, A. H. Said, and D. Reznik, *Phys. Rev. Lett.* **107**, 107403 (2011).
- [48] Y. Song, S. Wu, X. Chen, Y. He, H. Uchiyama, B. Li, S. Cao, J. Guo, G. Cao, and R. Birgeneau, *Phys. Rev. B* **107**, L041113 (2023).
- [49] S. M. Souliou, T. Lacmann, R. Heid, C. Meingast, M. Frachet, X. Paolasini, A.-A. Haghighirad, M. Merz, A. Bosak, and M. Le Tacon, *Phys. Rev. Lett.* **129**, 247602 (2022).
- [50] P. Upreti, M. Krogstad, C. Haley, M. Anitescu, V. Rao, L. Poudel, O. Chmaissem, S. Rosenkranz, and R. Osborn, *Phys. Rev. Lett.* **128**, 095701 (2022).
- [51] A. Baron, Y. Tanaka, S. Goto, K. Takeshita, T. Matsushita, and T. Ishikawa, *Journal of Physics and Chemistry of Solids* **61**, 461 (2000).
- [52] J. Lamsal and W. Montfrooij, *Phys. Rev. B* **93**, 214513 (2016).
- [53] H. C. Robarts, M. Barthélemy, K. Kummer, M. García-Fernández, J. Li, A. Nag, A. C. Walters, K. J. Zhou, and S. M. Hayden, *Phys. Rev. B* **100**, 214510 (2019).
- [54] P. Giannozzi, S. Baroni, N. Bonini, and *et al.*, *Journal of Physics: Condensed Matter* **21**, 395502 (2009).
- [55] J. P. Perdew, K. Burke, and M. Ernzerhof, *Phys. Rev. Lett.* **77**, 3865 (1996).